Spatially-Resolved Investigation of the Water Inhibition of Methane Oxidation over Palladium

Ciaran Coney[1], Cristina Stere[2], Paul Millington[3], Agnes Raj[3], Sam Wilkinson[4], Michael Caracotsios[5], Geoffrey McCullough[6], Christopher Hardacre[2], Kevin Morgan[1], David Thompsett[3], Alexandre Goguet[1]*

[1]*School of Chemistry and Chemical Engineering, Queen's University Belfast, Belfast, BT9 5AG, United Kingdom*
[2] *School of Chemical Engineering and Analytical Science, University of Manchester, Manchester, M13 9PL, United Kingdom*
[3] *Johnson Matthey Technology Centre, Blounts Court, Sonning Common, Reading RG4 9NH, United Kingdom*
[4] *Johnson Matthey Technology Centre, Belasis Avenue, Billingham, TS23 1LB, United Kingdom*
[5] *Chemical Engineering Department, University of Illinois at Chicago, Chicago, Illinois 60607, USA*
[6] *School of Mechanical and Aerospace Engineering, Queen's University Belfast BT9 5AH, United Kingdom*

*a.goguet@qub.ac.uk

Experimental

Prior to each experimental test, the monolith core was pre-treated for 2 hours using a 2 L.min^{-1} gas stream containing 20 v/v% O_2 in Ar, at a furnace temperature of 450°C, corresponding to a space velocity of *ca.* 23,000 h^{-1} at the terminal measurement position. Following the pre-treatment process, a three hour baseline was carried utilising a 2 L.min^{-1} flow of 100 %v/v Ar, to ensure a stable background had developed on the mass spectrometer. The thermocouple probes T_1-T_3, and open-ended fused silica capillaries C_1-C_3 were positioned 3 mm in front of the inlet of the monolith core so as to record the inlet baseline concentrations. An automated MATLAB program controlled the selection of the open ended capillaries, permitting each radially distributed capillary to sample gas flow in adjacent channels in a series based sampling routine. Each capillary sampled gas for a fixed time of 270 s, with the first 10 s of each capillary's sampling time discarded to allow sufficient time to remove any gaseous artefacts remaining from the previous capillary. The remaining gas composition was averaged over the 260 s time frame, to yield one data point per capillary. Succeeding the baseline test, the appropriate steady state reaction conditions, summarised in Table S1, were set up on the SpaciMS system, with the remainder of the gas flow being made

up of CH_4, O_2 and Ar. Again, the inlet feed concentrations were recorded 3 mm in front of the inlet of the core, utilising the same automated capillary sampling method and data averaging technique. The probes were translated axially inside the monolith channels, scanning positions between 0-60 mm, with an axial resolution of 3 mm. The movement of the probes was actuated by a Thorlabs APT Microstepping Controller, controlled via a MATLAB routine permitting the programming of the initial and final probe positions, axial step size, total step time and settling time.

Table S1 Experimental test conditions inclusive of 12% O_2, 4000 ppm CH_4 and Ar balance

H$_2$O Concentrations (%v/v)	Temperature (°C)		
	400	**425**	**450**
0 %v/v	400_0 H2O	425_0 H2O	450_0 H2O
1 % v/v	400_1 H2O	425_1 H2O	450_1 H2O
5 % v/v	400_5 H2O	425_5 H2O	450_5 H2O
10 % v/v	400_10 H2O	425_10 H2O	450_10 H2O

Kinetics Investigation

Both reactant and product inhibition have the potential to greatly influence the rate of CH_4 oxidation reaction. To investigate the effect of reactant concentration on reaction order, five different inlet CH_4 concentrations were tested in the presence of 12 %v/v O_2 under dry conditions at a steady state furnace temperature of 400 °C, detailed in Fig. S1. Considering the five tested conditions, the observed experimentally measured gas temperature in the central monolith channel ranged from 405-517 °C, probed over an axial range of 57 mm as shown by Fig. S2. It was possible to calculate the rate of CH_4 removal at various axial locations by converting the x-axis to residence time (s), converting the y-axis to CH_4 concentration (mol.m^{-3}), and subsequently differentiating the profile curves to obtain the rate (mol.m^{-3}.s^{-1}). The order of reaction with respect to CH_4 was initially assessed at three instances; channel inlet, reference temperature (T_{ref}) and a position corresponding to 80%

CH$_4$ conversion. T$_{ref}$ is calculated via Eqn. S1, and effectively represents the average gaseous temperature of the temperature profile for the respective reactions, where n is equal to the number of axial sample points.
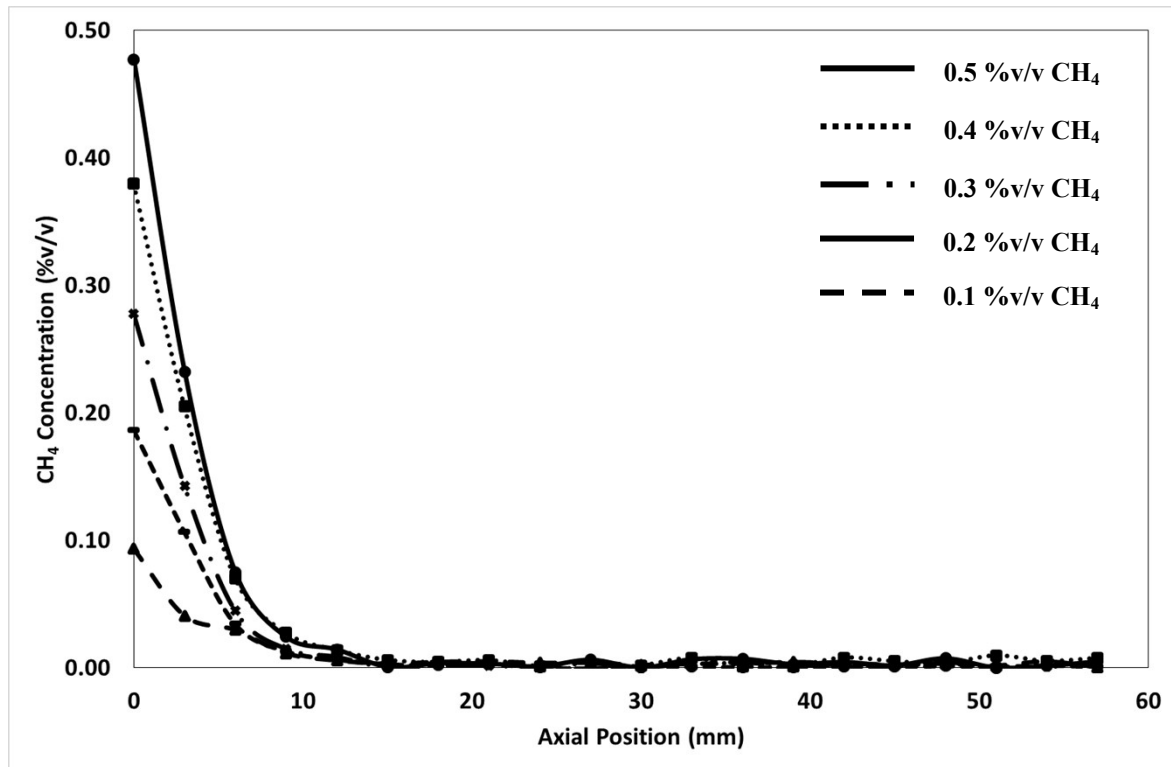
Fig. S1 CH$_4$ concentration as a function of axial position for steady state profile reactions employing feed concentrations of 12 %v/v O$_2$ and 0-0.5 %v/v CH$_4$.

$$T_{ref} = \frac{n}{\sum_{i=1}^{n} \frac{1}{T_i}}$$

(Eqn S1.)

To assess the approximate reaction order with respect to CH$_4$, it was important to consider the catalyst temperature at the axial points at which the reaction rates were being extracted, as temperature differences would influence the observed reaction rate due to the temperature dependence of the Arrhenius equation. Based on the temperature profiles in Fig. S2, it was judged that the reaction rate corresponding to the inlet of the monolith channel was the most suitable location at which to extract the reactions rates, owing to the fact that the gaseous temperatures were comparable at an axial positions of zero. At axial positions

corresponding to T_{ref} and 80% CH_4 conversion, relatively large gaseous temperature differences were realised between the reactions employing different CH_4 feed concentrations, therefore observed reaction rates at these positions were not appropriate as a metric for comparing reaction order. Calculation of the Weisz-Prater criteria suggested that internal mass transfer limitation was likely to occur at the inlet of the monolith channel under dry
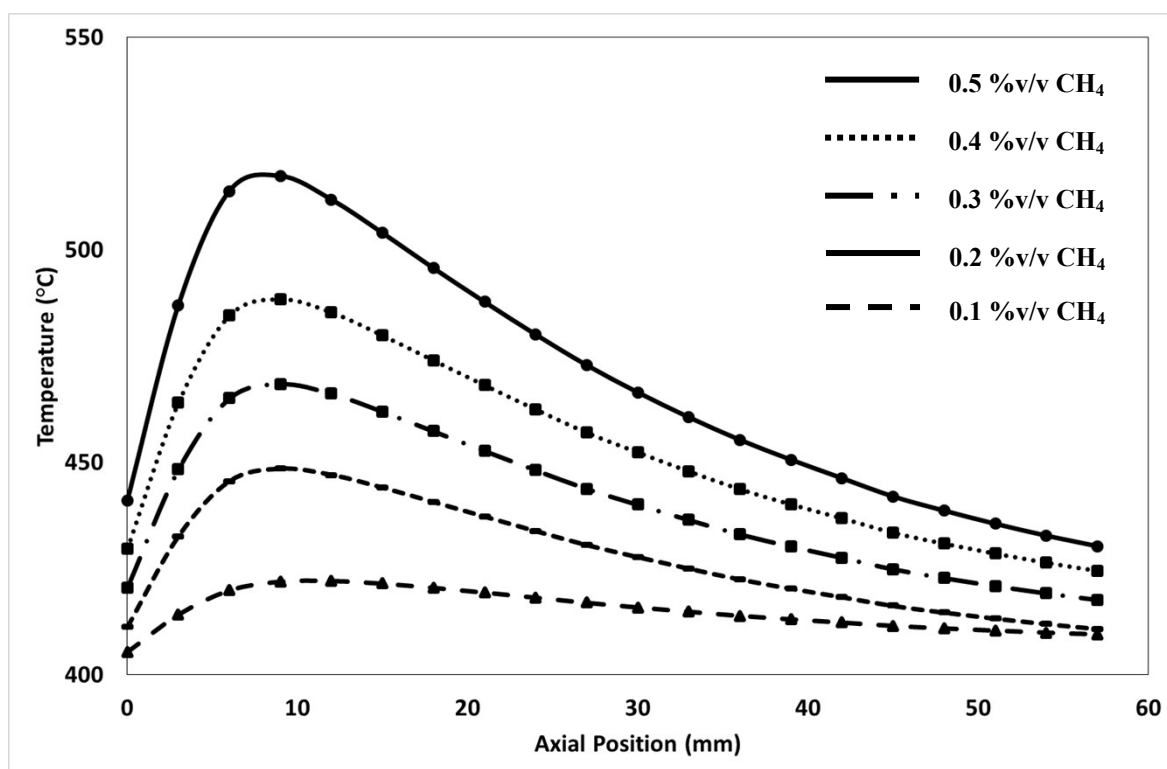
Fig. S2 Gas temperature of central monolith channel as a function of axial position for steady state profile reactions employing feed concentrations of 12 %v/v O_2 and 0-0.5 %v/v CH_4.

conditions. As the CH_4 reaction rate was derived from the experimentally observed rate, and the extent of internal mass transfer limitation was calculated to be very similar at all CH_4 feed concentrations, calculation of the reaction order with respect to CH_4 using this method was deemed satisfactory.

Fig. S3 displays a plot of $Ln(CH_4$ reaction rate) vs $Ln(CH_4$ concentration), utilising the resultant gradient (n) to calculate the reaction order with respect to CH_4, in accordance with Eqn. S2. The calculated gradient of 0.979 approximately equates to a value of 1,

indicating that the reaction order is first order with respect to CH_4, an observation supported by many authors in literature.[1,2,3,4]

$$Ln(CH_4 Reaction\ Rate) = nLn(CH_4\ Concentration) + Ln(k) \qquad \text{(Eqn. S2)}$$
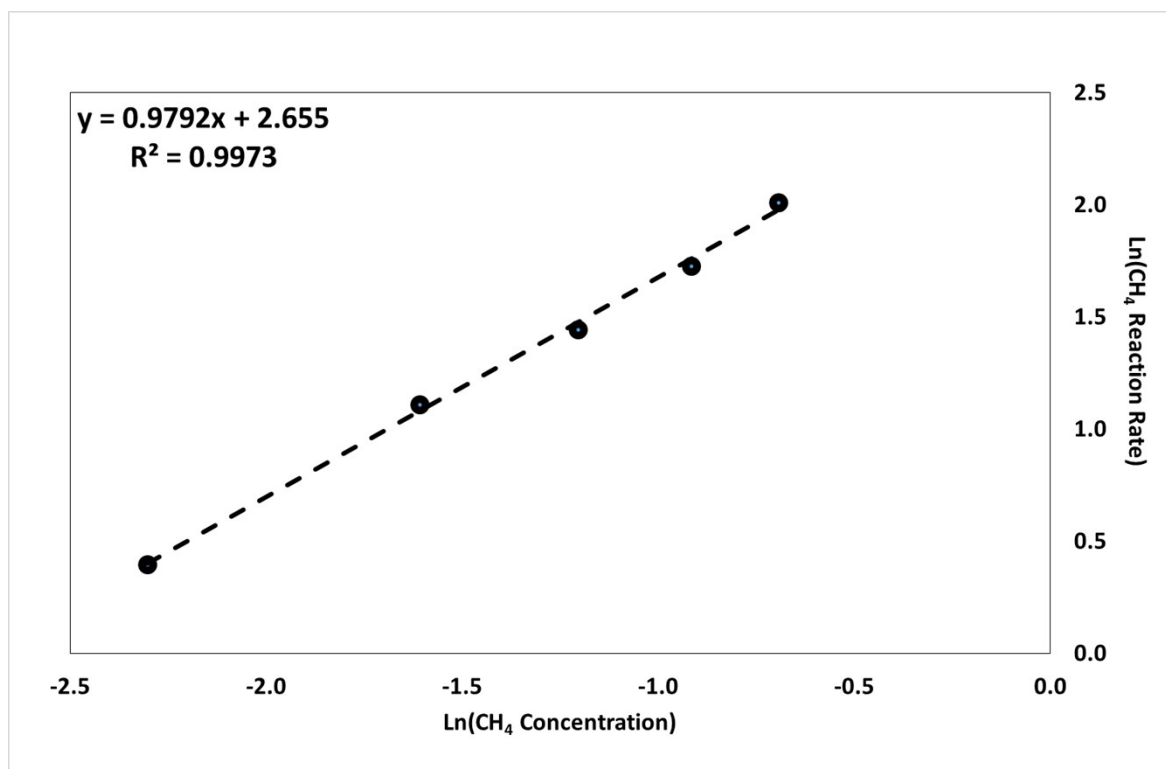
Fig. S3 Ln(CH_4 Reaction Rate) as a function of Ln(CH_4 Concentration)

Under specific conditions, the effect of CO_2 inhibition on CH_4 oxidation reaction has been shown to contribute to a reduction in the apparent observed catalytic activity of the Pd/Al_2O_3 monolithic system.[4-5] To investigate potential CO_2 inhibition for the catalyst employed in this work, five light-off reactions were carried out at an axial position of 25 mm from the inlet of the central monolith channel. Prior to catalytic testing, the catalyst was pre-treated at 450 °C in a 20 %v/v O_2 stream for 2 hours to remove the any adsorbed carbon based species. The catalyst was subsequently cooled to 50 °C at which point it was subjected to feed conditions of 4000 ppm CH_4, 12 %v/v O_2 and CO_2 concentrations varying from 0-1.5 %v/v. For each CO_2 feed concentration a furnace temperature ramp rate of 2 °C.min^{-1} was applied, raising the temperature from 50 °C to 450 °C. The results of the light-off tests are

displayed in Fig. S4, detailing the CH_4 concentration as a function of gaseous temperature recorded 25 mm from the inlet of an adjacent central channel. For each CO_2 feed concentration the rate of reaction is calculated at three points corresponding to temperatures of 300, 350 and 425 °C, summarised in Table S2. It is apparent from the observed rates of CH_4 removal and consistent overlap of the light-off profiles in Fig. S4, changing the inlet CO_2 concentration had a negligible effect on the rate of reaction, indicating that CO_2 inhibition is not significant. If CO_2 was contributing significantly to inhibition of the methane oxidation process, the light-off curve would be expected to shift to the right at higher feed CO_2 concentrations, as higher catalyst temperatures would be required to bring about the same level of conversion as the non-inhibited reaction.
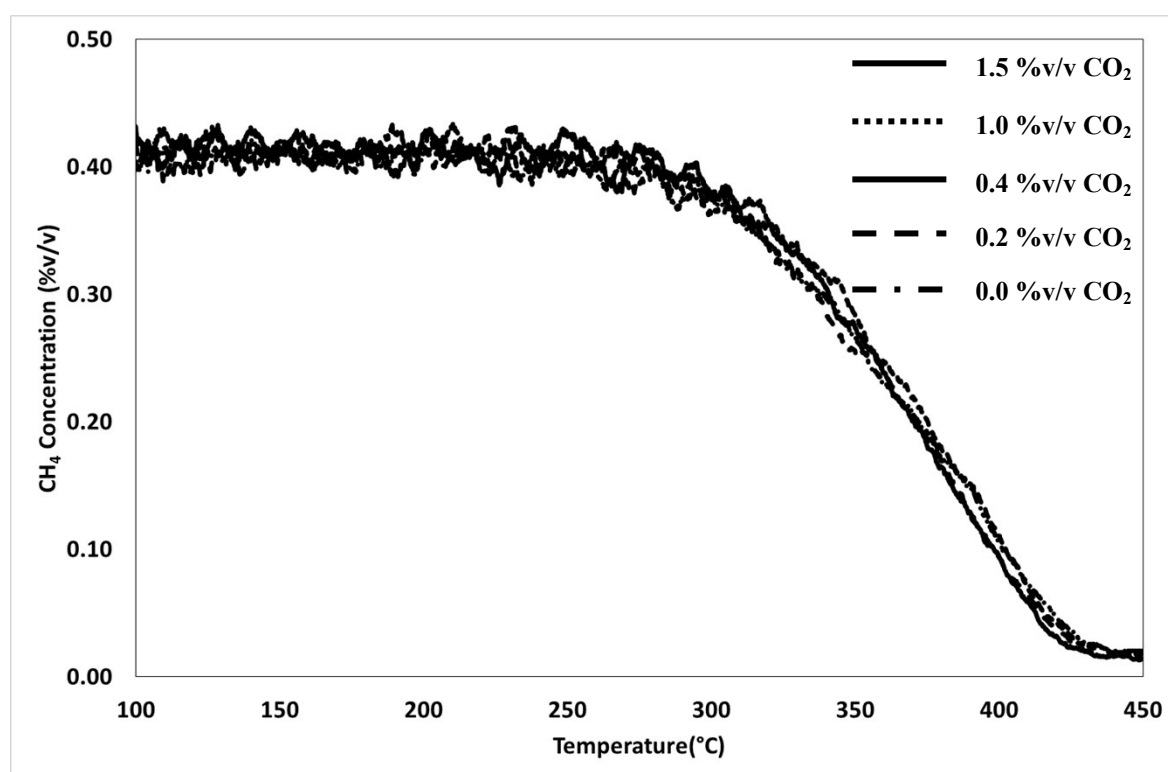
Fig. S4 CH_4 concentration as a function of temperature for light-off reactions employing feed concentrations of 4000ppm CH_4, 12 %v/v O_2 and 0-1.5 %v/v CO_2.

Table S2 Calculated rate of CH_4 oxidation at 300 °C, 350 °C and 425 °C for CO_2 concentrations of between 0-1.5 % v/v

CO_2 Concentrations	CH_4 Rate of Reaction ($x10^{-4}$ mol.m^{-3}.s^{-1})		
	T300	T350	T425
0 %v/v	3.38	7.83	3.34
0.2 % v/v	4.03	7.43	2.73
0.4 % v/v	4.26	7.72	2.78
1 % v/v	3.91	7.77	3.01
1.5 % v/v	3.97	7.58	2.80

The effect of H_2O inhibition on CH_4 oxidation occurring on a Pd/Al_2O_3 monolithic catalyst was investigated by performing 4 light-off reactions at an axial position of 25 mm from the inlet of the central monolith channel. Prior to catalytic testing, adsorbed surface species were removed from the catalyst via pre-treatment at 450 °C in a 20 %v/v O_2 stream for 2 hours. The catalyst was subsequently cooled to 50 °C at which point the catalyst was subjected to feed conditions of 4000 ppm CH_4 and 12 %v/v O_2 and H_2O concentrations varying from 0-10 %v/v. For each H_2O feed concentration a furnace temperature ramp of 2 °C.min^{-1} was applied, raising the temperature from 50 °C to 550 °C. The results of the light-off tests are displayed in Fig. S5, detailing the CH_4 concentration as a function of the gas temperature recorded 25 mm from the inlet of an adjacent central channel. From inspection of Fig. S5, increasing H_2O feed concentrations has the effect of shifting the light-off curve to the right i.e. increasing the temperature at which 50% CH_4 conversion occurs. The inhibitory effect is hypothesised to be caused by the formation of a surface hydroxyl species on the dispersed Pd, limiting the rate of CH_4 oxidation reaction. The inhibitory effect is enhanced at higher H_2O feed concentrations due to shift in equilibrium surface coverage of the adsorbed hydroxyl species, accumulating in the axial region between the inlet and 25 mm in the central channel of the monolith core.
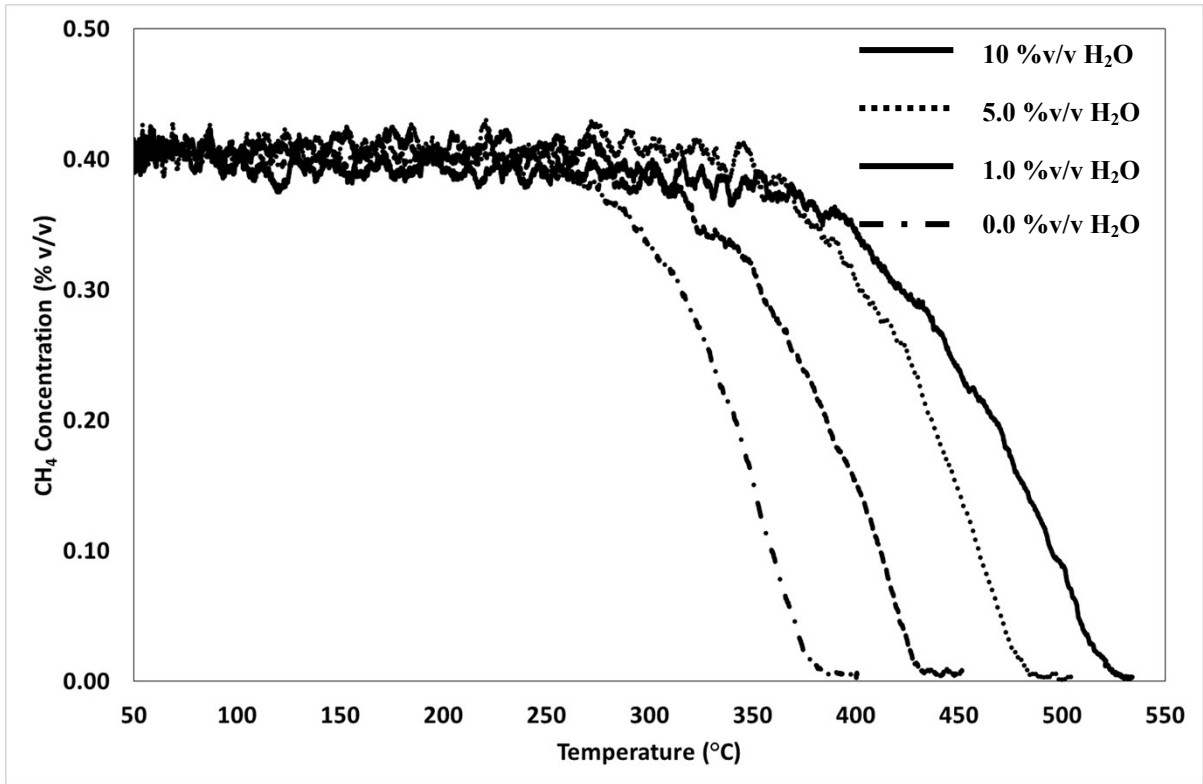
Fig. S5 CH$_4$ concentration as a function of temperature for light-off reactions employing feed concentrations of 4000ppm CH$_4$, 12 %v/v O$_2$ and 0-10 %v/v H$_2$O

Modelling – Re-parameterisation

Rate constant (k_r) and equilibrium constants (K_i) are incorporated into rate expressions via Arrhenius and van't Hoff equations, Eqns. S3 and S4 respectively. Reparametrized forms of Eqns. S3 and S4 were applied to the model during the parameter estimation routine, exemplified by Eqns. S8 and S9. The subscript i denotes the inhibiting species CO_2, H_2O or CH_4.

$$k_r = k_0 e^{\left(\frac{-Ea}{R}\left(\frac{1}{T_2} - \frac{1}{T_1}\right)\right)}$$ (Eqn. S3)

$$K_2 = K_{0,i} e^{\left(\frac{-\Delta H_r}{R}\left(\frac{1}{T_2} - \frac{1}{T_1}\right)\right)}$$ (Eqn. S4)

$$k_r = k_{ref} e^{\left(\frac{-E_a}{RT^*}\right)}$$ (Eqn. S5)

where:

$$k_{ref} = k_0 e^{\left(\frac{-Ea}{RT_{ref}}\right)}$$ (Eqn. S6)

$$\frac{1}{T^*} = \frac{1}{T} - \frac{1}{T_{ref}}$$ (Eqn. S7)

$$k_r = Par(1) e^{\left(Par(2)\left(\frac{T_{ref}}{T} - 1\right)\right)}$$ (Eqn. S8)

$$K_2 = Par(3) e^{\left(Par(4)\left(\frac{T_{ref}}{T} - 1\right)\right)}$$ (Eqn. S9)

Kinetic Model Derivations

Models 1-8 were hypothesised in the work of Shahrestani[16] to describe the behaviour of the water inhibited methane oxidation reaction on Pd/Al_2O_3 catalysts. Each model assumes that the initial hydrogen atom cleavage from the CH_4 molecule is irreversible and is the rate determining step. The models also assume that the reversible adsorption of $H_2O_{(g)}$ occurs on oxygen vacancy sites, whilst $H_2O_{(ads)}$ reversibly reacts with PdO to form adsorbed hydroxyl groups. The mathematically derived expressions for each model are subsequently described

hereafter, beginning with the assumption of elementary reactions between the gaseous reactants and products with the active sites (S), represented by Eqns. S10-S13.

$$CH_4 + S \rightleftharpoons S_{CH4}$$ (Eqn S10)

$$O_2 + S \rightleftharpoons S_{O2}$$ (Eqn S11)

$$CO_2 + S \rightleftharpoons S_{CO2}$$ (Eqn S12)

$$H_2O + S \rightleftharpoons S_{H2O}$$ (Eqn S13)

The total concentration of available sites for adsorption of all available gaseous components can be calculated by the site balance detailed by Eqn. S14, where $[S_{CH4}]$, $[S_{O2}]$, $[S_{CO2}]$ and $[S_{H2O}]$ represent the respective concentration of CH_4, O_2, CO_2 and H_2O adsorption sites on the catalyst surface. $[S_T]$ and $[S_{free}]$ represent the total and free concentration of adsorption sites respectively. The site concentrations are converted into fractions of the total number of available adsorption sites $[S_T]$ by applying Eqn. S15, resulting in Eqn. S16.

$$[S_T] = [S_{free}] + [S_{CH4}] + [S_{O2}] + [S_{CO2}] + [S_{H2O}]$$ (Eqn S14)

$$\theta_{CH4} = \frac{[S_{CH4}]}{[S_T]}$$ (Eqn S15)

$$1 = \theta_{free} + \theta_{CH4} + \theta_{O2} + \theta_{CO2} + \theta_{H2O}$$ (Eqn S16)

The change in concentration of each species with time is assumed to be dictated by the adsorption equilibrium process, Eqns. S17-S20, where it is supposed that the forward adsorption process $(k_{1,2,3,4})$ is non-dissociative demonstrating first order behaviour with respect to the component in question. The desorption process is exhibited by the backward process $(k_{-1,-2,-3,-4})$ with the equilibrium presented by Eqn. S21.

$$r_{CH4} = \frac{dCH_4}{dt} = k_1[CH_4][S] - k_{-1}[S_{CH4}]$$ (Eqn S17)

$$r_{O2} = \frac{dO_2}{dt} = k_2[O_2][S] - k_{-2}[S_{O2}]$$ (Eqn S18)

$$r_{CO2} = \frac{dCO_2}{dt} = k_3[CO_2][S] - k_{-3}[S_{CO2}]$$

(Eqn S19)

$$r_{H2O} = \frac{dH_2O}{dt} = k_4[H_2O][S] - k_{-4}[S_{H2O}]$$

(Eqn S20)

$$K_{CH4} = \frac{k_1}{k_{-1}} = \frac{[S_{CH4}]}{[CH_4][S]}$$

(Eqn S21)

$$[S_{CH4}] = K_{CH4}[CH_4][S]$$

(Eqn S22)

$$\theta_{CH4} = K_{CH4}[CH_4]\theta_{free}$$

(Eqn S23)

$$\theta_{O2} = K_{O2}[O_2]\theta_{free}$$

(Eqn S24)

$$\theta_{CO2} = K_{CO2}[CO_2]\theta_{free}$$

(Eqn S25)

$$\theta_{H2O} = K_{H2O}[H_2O]\theta_{free}$$

(Eqn S26)

The steady state approximation is applied to the adsorption-desorption process, assuming that the forward and backward reactions are in equilibrium with no accumulation occurring. The result of the steady state approximation leads to the formation of Eqn. S22, where the concentration of adsorbed component is a function of equilibrium constant (K_i), gaseous concentration ([i]) and concentration of free active sites ([S_{free}]). By combining Eqn. S22 with Eqn. S15 for each component, Eqns. S23-26 are formed, detailing the fraction of surface coverage as a function of equilibrium constant (K_i), gaseous concentration ([i]) and fraction of free active sites (θ_{free}). By expressing the surface coverage in terms of fraction of total available sites, as opposed to surface concentration of available sites, it avoids the complication of having to calculate the surface concentration of each adsorbed species. Eqns.. S23-S26 combined with Eqn S16 gives the fraction of free sites as a function of the surface coverage of all other adsorbed components.

$$\theta_{free} = \frac{1}{(1 + K_{CH4}[CH_4] + K_{O2}[O_2] + K_{CO2}[CO_2] + K_{H2O}[H_2O])}$$
(Eqn S27)

Eqn S27 was used to derive a number of global kinetic models based on different modes of reaction and various inhibiting components, detailed henceforth.

Models 3, 4 and 6

In the development of Models 3, 4 and 6, it was assumed that the CH_4 oxidation reaction was 1st order with respect to surface CH_4 concentration, zero order with respect to O_2 concentration and 2nd order with respect to a site-pair of active sites (PdO-PdO, PdO-O_v or O_v-O_v), culminating in Eqns. S28 – S31. As the surface coverage of CH_4 is dependent on two sites as opposed to one site, Eqn. S22 has been adapted to form Eqn. S29 which accounts for the presence of two catalytically active sites.

$$rate = k_r[S_{CH4}]$$ (Eqn S28)

$$[S_{CH4}] = K_{CH4}[CH_4][S]^2$$ (Eqn. S29)

$$rate = k_r K_{CH4}[CH_4]\theta_{free}^2$$ (Eqn S30)

$$rate = \frac{k_r K_{CH4}[CH_4]}{(1 + K_{CH4}[CH_4] + K_{O2}[O_2] + K_{CO2}[CO_2] + K_{H2O}[H_2O])^2}$$ (Eqn S31)

Model 3 assumes that the surface concentrations of CH_4, CO_2 and O_2 are negligible due to fast desorption processes, thus Eqn. S31 simplifies to Eqn. S32 where only H_2O is hypothesised to inhibit the reaction.

$$rate = \frac{k_r K_{CH4} K_{O2}[CH_4][O_2]}{(1 + K_{H2O}[H_2O])^2}$$ (Eqn S32)

Model 4 assumes that the surface concentrations of CO_2 and O_2 are negligible due to fast desorption processes, thus Eqn. S31 simplifies to Eqn. S33 where both CH_4 and H_2O are reflective of inhibition during the reaction.

$$rate = \frac{k_r K_{CH4} K_{O2}[CH_4][O_2]}{(1 + K_{CH4}[CH_4] + K_{H2O}[H_2O])^2}$$ (Eqn S33)

Model 6 assumes that the surface concentration of CH_4 and O_2 are negligible due to fast desorption processes, thus Eqn. S31 simplifies to Eqn. S34 where both CO_2 and H_2O are reflective of inhibition during the reaction.

$$rate = \frac{k_r K_{CH4} K_{O2}[CH_4][O_2]}{(1 + K_{CO2}[CO_2] + K_{H2O}[H_2O])^2}$$
(Eqn S34)

Models 2 and 5

In the derivation of Models 2 and 5, it was assumed that the reaction was 1st order with respect to the surface CH_4 concentration, requiring adsorbed CH_4 to react with gaseous O_2, resulting in Eqns. S35 – S37.

$$rate = k_r[S_{CH4}]$$
(Eqn S35)

$$rate = k_r K_{CH4}[CH_4]\theta_{free}$$
(Eqn S36)

$$rate = \frac{k_r K_{CH4}[CH_4]}{1 + K_{CH4}[CH_4] + K_{O2}[O_2] + K_{CO2}[CO_2] + K_{H2O}[H_2O]}$$
(Eqn S37)

In a similar manner to the derivation of Model 3, Model 2 assumes that the surface concentrations of CH_4, CO_2 and O_2 are negligible due to fast desorption processes, yielding Eqn. S38, where only H_2O is attributed to an inhibiting species.

$$rate = \frac{k_r K_{CH4}[CH_4]}{1 + K_{H2O}[H_2O]}$$
(Eqn S38)

Model 5 assumes that the surface concentration of CH_4 and O_2 are negligible, reducing Eqn. S31 to Eqn. S39, where CO_2 and H_2O account for the inhibiting species.

$$rate = \frac{k_r K_{CH4}[CH_4]}{1 + K_{CO2}[CO_2] + K_{H2O}[H_2O]}$$
(Eqn S39)

Model 7

The derivation of Mars van Krevelen based Model 7, begins by describing the mechanism using three reaction steps; reaction of CH_4 with the oxidised catalyst (Eqn. S40); reaction of the reduced form of the catalyst with gaseous O_2 (Eqn. C41); and reaction of the reduced form of the catalyst with gaseous H_2O (Eqn. C42).

$$Cat_{Ox} + R \rightarrow R-O + Cat_{Red} \tag{Eqn. S40}$$

$$Cat_{Red} + O_2 \rightarrow Cat_{Ox} \tag{Eqn. S41}$$

$$Cat_{Red} + H_2O \rightleftharpoons Cat_{H_2O} \tag{Eqn. S42}$$

Several assumptions were then made:

- The reaction was assumed to be first order with respect to CH_4 and first order with respect to surface coverage of oxygen.

- Lattice oxygen ions were supposed to take part in the oxidation of CH_4.

- The rate of surface re-oxidation is proportional to P_{O2} and to the concentration of active sites not covered by oxygen or water.

The total fractional coverage of catalytic sites is represented by the summation of fractional O_2 surface coverage (θ_{O2}), fractional H_2O surface coverage (θ_{H2O}) and fractional reduced site surface coverage (θ_{Red}), detailed by Eqn. S43. Surface coverage of CO_2 is assumed to be insignificant.

$$\theta_{Ox} + \theta_{Red} + \theta_{H_2O} = 1 \tag{Eqn. S43}$$

$$\theta_{Red} = 1 - \theta_{Ox} - \theta_{H_2O} \tag{Eqn. S44}$$

$$\theta_{Ox} = 1 - \theta_{Red} - \theta_{H_2O} \tag{Eqn. S45}$$

Eqn. S40 assumes that the reaction is 1st order with respect to CH_4 concentration and 1st order with respect to O_2 surface coverage θ_{O2}. Therefore, the reduction rate of catalytic sites is represented by Eqn. S46.

$$r_{Red} = k_{Red}[CH_4]\theta_{Ox} \tag{Eqn. S46}$$

Eqn. S41 assumes that the rate of oxidation is 1st order with respect to O_2 concentration and 1st order with respect to reduced site surface coverage θ_{Red}. Therefore, the oxidation rate of catalytic sites is represented by Eqn. S47.

$$r_{Ox} = k_{Ox}[O_2]\theta_{Red} \tag{Eqn. S47}$$

Eqn. S42 assumes that adsorption of H_2O on reduced catalytic sites occurs reversibly, with the forward adsorption process (k_d) 1st order with respect to H_2O concentration and 1st order with respect to reduced site surface coverage θ_{Red}. The backward desorption process is assumed to occur via 1st order kinetics with respect to surface coverage of H_2O (θ_{Red}). Therefore, the H_2O sorption rate is represented by Eqn. S48.

$$r_{H_2O} = k_d[H_2O]\theta_{Red} - k_i\theta_{H_2O} \tag{Eqn. S48}$$

Assuming the steady-state approximation applies, the surface coverage of H_2O is represented by Eqn. S49, in which K_{H2O} equates to the equilibrium constant k_d/k_i.

$$\theta_{H_2O} = K_{H_2O}[H_2O]\theta_{Red} \tag{Eqn. S49}$$

Re-oxidation of the catalyst, detailed in Eqn. S47, is assumed to be occurring simultaneously to the reduction of the catalyst via reaction with CH_4, detailed in Eqn. S46. Both processes are hypothesised to be in equilibrium with each other, therefore Eqn. S50 applies.

$$k_{Red}[CH_4]\theta_{Ox} = k_{Ox}[O_2]\theta_{Red} \tag{Eqn. S50}$$

By substituting Eqn. S45 into Eqn. S50, whilst if complete oxidation of one CH_4 molecule requires β molecules of O_2 to react (Eqn. S51), Eqn. S52 is derived. Eqn. S52 assumes that H_2O inhibition is acting on the reduction sites via inclusion of the fractional coverage of H_2O in the r_{red} portion of the rate equation i.e. sites at which CH_4 oxidation is occurring.

$$r_{Red} = \frac{r_{Ox}}{\beta} = r \qquad \text{(Eqn. S51)}$$

$$\beta k_{Red}[CH_4](1 - \theta_{Red} - \theta_{H_2O}) = k_{Ox}[O_2]\theta_{Red} \qquad \text{(Eqn. S52)}$$

Stoichiometric CH_4 oxidation requires two O_2 molecules per CH_4 molecule, therefore Eqn. S52 reduces to Eqn. S53.

$$k_{Red}[CH_4](1 - \theta_{Red} - \theta_{H_2O}) = \frac{1}{2}k_{Ox}[O_2]\theta_{Red} \qquad \text{(Eqn. S53)}$$

By expanding Eqn. S53 and inserting Eqn. S49 in terms of H_2O fractional coverage (Eqns. S54 – S56), Eqn. S56 is derived permitting subsequent rearrangement and factorisation to give the fractional reduced site surface coverage θ_{red} of the catalyst in terms of concentration of CH_4, O_2 and H_2O concentrations (Eqns. S57 – S58).

$$k_{Red}[CH_4] - k_{Red}[CH_4]\theta_{Red} - k_{Red}[CH_4]\theta_{H_2O} = \frac{1}{2}k_{Ox}[O_2]\theta_{Red} \qquad \text{(Eqn. S54)}$$

$$k_{Red}[CH_4] - k_{Red}[CH_4]\theta_{Red} - k_{Red}[CH_4]K_{H_2O}[H_2O]\theta_{Red} = \frac{1}{2}k_{Ox}[O_2]\theta_{Red} \qquad \text{(Eqn. S55)}$$

$$k_{Red}[CH_4] = \theta_{Red}(k_{Red}[CH_4] + k_{Red}[CH_4]K_{H_2O}[H_2O] + \frac{1}{2}k_{Ox}[O_2]) \qquad \text{(Eqn. S56)}$$

$$\theta_{Red} = \frac{k_{Red}[CH_4]}{k_{Red}[CH_4] + k_{Red}[CH_4]K_{H_2O}[H_2O] + \frac{1}{2}k_{Ox}[O_2]} \qquad \text{(Eqn. S57)}$$

$$\theta_{Red} = \frac{2k_{Red}[CH_4]}{2k_{Red}[CH_4](1 + K_{H_2O}[H_2O]) + k_{Ox}[O_2]} \qquad \text{(Eqn. S58)}$$

The overall rate expression for CH_4 oxidation reaction is derived by combing Eqn. S58 with Eqn. S47 to give Eqn. S59.

$$r = \frac{r_{Ox}}{2} = \frac{k_{Red}[CH_4]k_{Ox}[O_2]}{2k_{Red}[CH_4](1 + K_{H_2O}[H_2O]) + k_{Ox}[O_2]} \qquad \text{(Eqn. S59)}$$

Model 8

The derivation of Mars van Krevelen based Model 8, again describes the mechanism using three reaction steps; reaction of CH_4 with the oxidised catalyst (Eqn. S40); reaction of the reduced form of the catalyst with gaseous O_2 (Eqn. S41); and reaction of the reduced form of the catalyst with gaseous H_2O (Eqn. S42). The same assumptions as those applied to Eqns. S43 – S47 in Model 7 hold true, however H_2O inhibition is hypothesised to occur on catalytic re-oxidation sites as detailed by Eqn. S60.

$$r_{H_2O} = k_d[H_2O]\theta_{Ox} - k_i\theta_{H_2O}$$
(Eqn. S60)

Assuming the steady-state approximation applies, the surface coverage of H_2O is represented by Eqn. S61, in which K_{H2O} equates to the equilibrium constant k_d/k_i.

$$\theta_{H_2O} = K_{H_2O}[H_2O]\theta_{Ox}$$
(Eqn. S61)

Again, re-oxidation of the catalyst, detailed in Eqn. S47, is assumed to be occurring at the same time as the reduction of the catalyst via reaction with CH_4, detailed in Eqn. S46. Both processes are hypothesised to be in equilibrium with each other (Eqn. S50), and in combination with Eqn. S44 and Eqn. S51, Eqn. S62 is derived. Eqn. S62 assumes that H_2O inhibition is acting on the oxidation sites via inclusion of the fractional coverage of H_2O in the r_{ox} portion of the rate equation i.e. sites at which catalyst re-oxidation is occurring.

$$2k_{Red}[CH_4]\theta_{Ox} = k_{Ox}[O_2](1 - \theta_{Ox} - \theta_{H_2O})$$
(Eqn. S62)

Expanding Eqn. S62 and combining with Eqn. S61 (Eqns. S63 – S65), Eqn. S65 is derived permitting subsequent rearrangement and factorisation to give the fractional reduced site surface coverage θ_{ox} of the catalyst in terms of concentration of CH_4, O_2 and H_2O concentrations (Eqn. S66).

$$2k_{Red}[CH_4]\theta_{Ox} = k_{Ox}[O_2](1 - \theta_{Ox} - K_{H_2O}[H_2O]\theta_{Ox})$$
(Eqn. S63)

$$2k_{Red}[CH_4]\theta_{Ox} = k_{Ox}[O_2] - k_{Ox}[O_2]\theta_{Ox} - k_{Ox}[O_2]K_{H_2O}[H_2O]\theta_{Ox}$$

(Eqn. S64)

$$\theta_{Ox}(2k_{Red}[CH_4] + k_{Ox}[O_2] + k_{Ox}[O_2]K_{H_2O}[H_2O]) = k_{Ox}[O_2]$$

(Eqn. S65)

$$\theta_{Ox} = \frac{k_{Ox}[O_2]}{2k_{Red}[CH_4] + k_{Ox}[O_2] + k_{Ox}[O_2]K_{H_2O}[H_2O]}$$

(Eqn. S66)

The overall rate expression for CH$_4$ oxidation reaction is derived by combing Eqn. S66 with Eqn. S46 to give Eqn. S68.

$$r = r_{Red} = \frac{k_{Red}[CH_4]k_{Ox}P_{O_2}}{2k_{Red}[CH_4] + k_{Ox}[O_2] + k_{Ox}[O_2]K_{H_2O}[H_2O]}$$

(Eqn. S67)

$$r = \frac{k_{Red}[CH_4]k_{Ox}[O_2]}{2k_{Red}[CH_4] + k_{Ox}[O_2](1 + K_{H_2O}[H_2O])}$$

(Eqn. S68)

External Heat and Mass Transfer

With catalytic chemical reactions taking place within the wall of the monolith channel, the transport of gaseous reactants from the bulk gaseous phase to wash coat has the potential to produce transverse concentration and temperature gradients within the channel. The existence of transverse concentration and temperature gradients are dictated by the ratio of external mass and heat transfer across the channel relative to the removal of reactants and subsequent generation of heat from catalytic chemical reaction in the wash coat. It is well documented that the operating temperature influences the extent of the transverse gradients produced, with low operating temperature generally favouring relatively small transverse gradients (uniform concentration and temperature distribution) and high temperatures supporting relatively large transverse gradients (non-uniform concentration and temperature distribution). Therefore, in the main, low operating temperatures are reflective of kinetically controlled regimes whilst high operating temperatures indicate mass transfer controlled regimes, however channel shape and dimensions, flow regime, wash coat uniformity and axial co-ordinate can all impact on external heat and mass transfer.

The most common approaches employed in the literature to assess external heat and mass transfer in monolith catalysts, involve the use of lumped parameter models, distributed models and empirically derived correlations. Lumped parameter and distributed models incorporating heat and mass transfer are generally applied to 2D and 3D models encompassing multiple channels, whereas empirical correlations are mostly used to describe two-phase 1D single channel models. In this work, the external heat and mass transfer effects have been assessed by employing empirical correlations derived by Forzatti *et al.*.[6] In their work, Eqn. S77 were developed by solving the Graetz problem under an assumption of constant wall temperature. The authors concluded that Eqn. S69 could be considered

analogous to Eqn. S70 under conditions where the Schmidt number (Eqn. S71) is equal to the Prandtl number (Eqn. S73) i.e. molecular diffusion rate is equal to thermal diffusion rate.

$$Sh = 2.977 + 6.874\left(\left(\frac{z}{D_h ReSc}\right)^{-0.488} exp\left(\frac{-57.2z}{D_h ReSc}\right)\right) \qquad \text{(Eqn S69)}$$

$$Nu = 2.977 + 6.874\left(\left(\frac{z}{D_h RePr}\right)^{-0.488} exp\left(\frac{-57.2z}{D_h RePr}\right)\right) \qquad \text{(Eqn S70)}$$

$$Sc = \frac{\mu_g}{\rho_g D_{eff}} \qquad \text{(Eqn S71)}$$

$$Re = \frac{\rho_g v_m D_h}{\mu_g} \qquad \text{(Eqn S72)}$$

$$Pr = \frac{\mu_g C_{p,g}}{k_m} \qquad \text{(Eqn S73)}$$

The external heat and mass transfer coefficients are calculated via Eqns. S75 and S74 respectively.

$$k_{m,A} = \frac{Sh\, D_{eff}\rho_g}{D_h} \qquad \text{(Eqn S74)}$$

$$h = \frac{Nu\, k_m}{D_h} \qquad \text{(Eqn S75)}$$

The presence of external mass transfer was evaluated using the Mears criterion, Eqn. S76. Similar to the Weisz-Prater criterion, the Mears criterion utilises the observed rate of reaction to assess whether external mass transfer limitations are likely to exist between the bulk gas phase and catalyst surface.

$$Mears\ criterion = \frac{L\, r'_p}{k_{m,A} C_{g,A}} \qquad \text{(Eqn S76)}$$

It has been proposed by Mears[7] that external mass transfer can be neglected for criteria values corresponding to less than 0.15. For Mears criterion values less than 0.15, Mears surmised that zero concentration gradient exists between bulk gas phase and external catalyst surface. External mass transfer coefficient was calculated via Eqn. S76, with observed reaction rate r'$_p$ determined via mathematical fitting, whilst characteristic length L and bulk $CH_{4,g}$ concentration were determined experimentally.
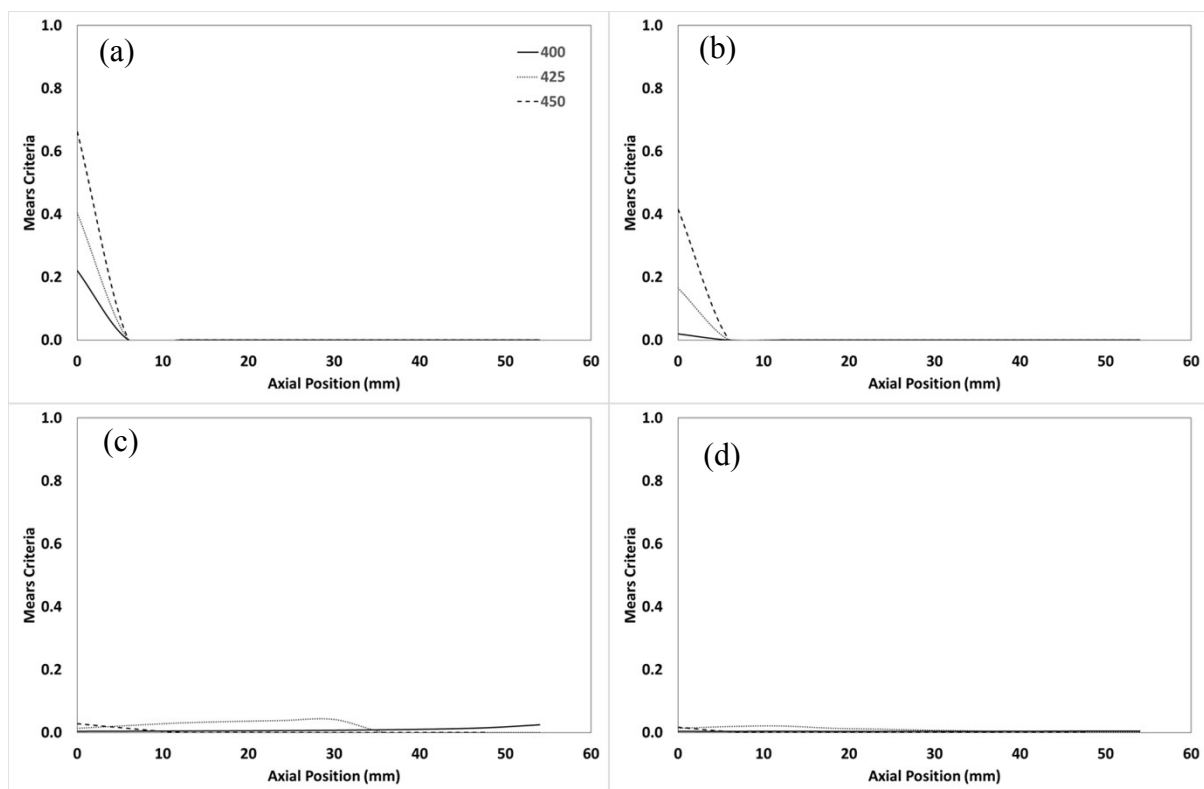
Fig. S6 Localised Mears criteria as a function of axial position, performed in the presence of 4000 ppm CH_4, 12 vol% O_2 and (a) 0 vol%, (b) 1 vol%, (c) 5 vol%, (d) 10 vol%.

Wash Coat Thickness
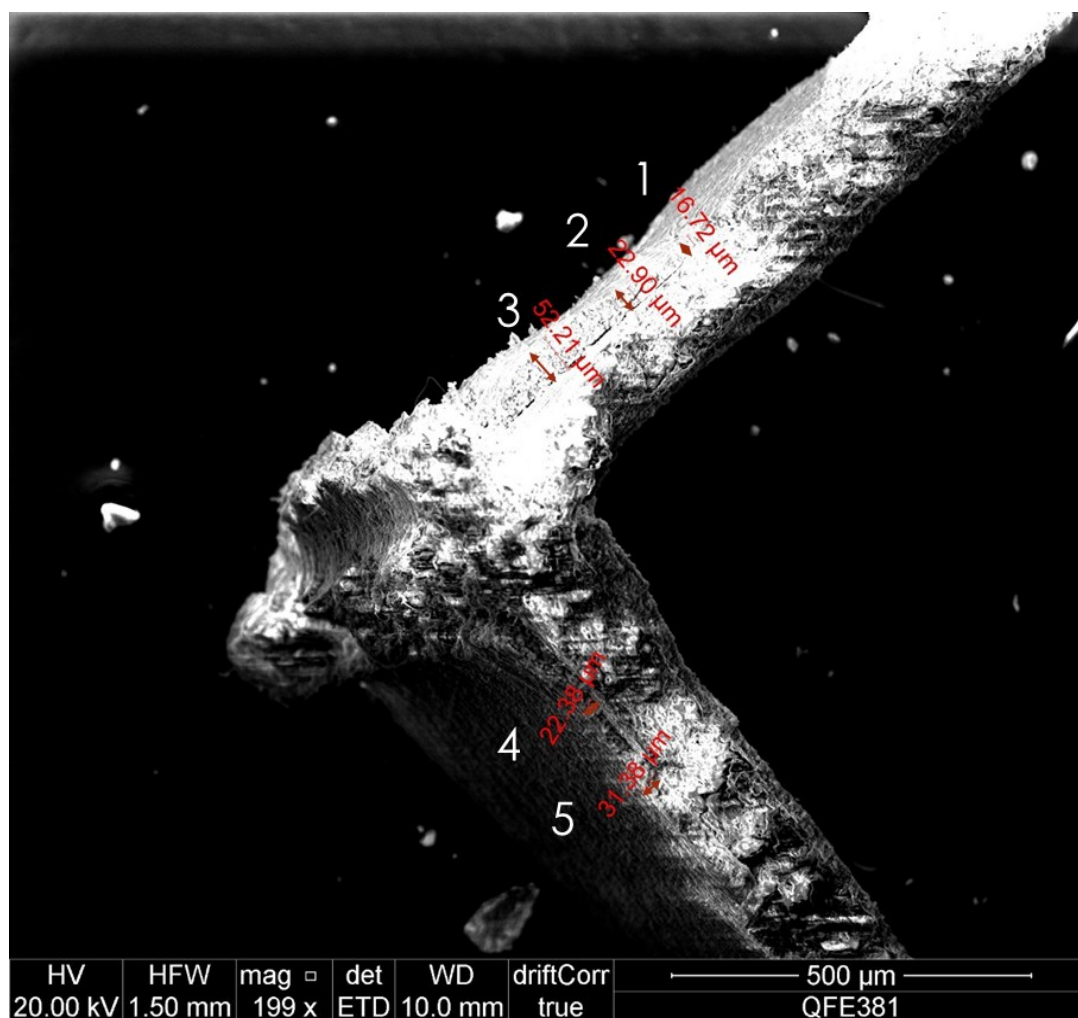
Fig. S7 Cross sectional SEM image of a sample of the central channel of the 3%Pd/Al$_2$O$_3$ monolith core, produced by ETD at a magnification of x199 and resolution of 1μs.

Scanning Electron Microscopy (SEM) was used to obtain an estimated value for the thickness of the 3%Pd/Al$_2$O$_3$ wash coat applied to the monolith core. A FEI Quanta FEG - Environmental SEM (Oxford Ex-ACT) was employed in ETD mode, utilising a magnification of x199 under high vacuum to visualise a cross section of a monolith channel. Fig. S7 displays a cross section of the corner of the central monolith channel, detailing the wash coat thickness at five measurement points, with the value for wash coat thicknesses summarised in Table S3.

Table S3 Wash coat thickness at multiple positions on the central monolith channel

Identifier	Wash Coat Thickness (mm)
1	16.72
2	22.90
3	52.21
4	22.38
5	31.38
Average	28.92

The five locations used for wash coat thickness determination, were selected with the view of assessing a range of transverse sites, as it is expected that the thickness will be greater closer to the corner of the channel, where circularity is often observed. The value for the average wash coat thickness was applied to the characteristic length (L) and utilised as an input in all modelling routines employed throughout this work.

Diffusivity

The effect of gaseous reactant and product diffusion plays an important role in heterogeneous reactions, as reactants must first diffuse from the bulk gas phase to the external catalyst surface i.e. external mass transfer, followed by intra-catalyst diffusion i.e. diffusion within the catalyst pores. In both cases, diffusion refers to the net transport of mass through a single phase, in this case gas, in which convective or mechanical mixing are not factors. Pressure, temperature, concentration and forced gradients can contribute to the driving force of diffusion, however in this work diffusional driving forces attributed to pressure, temperature and forced gradients have been disregarded due to the assumption that the system operates under *ca.* isobaric and isothermal conditions with no external force field gradients. The molecular diffusion of gaseous species in the bulk gas phase and macropores is calculated via Eqn. S77 developed by Fuller *et al.*[8,9], in which D_{AB} represents the binary diffusion coefficient of gas A in gas B ($cm^2.s^{-1}$), T_g represents the temperature of the bulk gas phase (K), P represents the system pressure (bar), M_A and M_B represents the molecular mass of gas A and B respectively and Σ_v represents the summation of the atomic diffusion volumes for gas A and B.

$$D_{AB} = \frac{0.00143 T_g^{1.75}}{P M_{AB}^{\frac{1}{2}} \left[(\Sigma_v)_A^{\frac{1}{3}} + (\Sigma_v)_B^{\frac{1}{3}} \right]^2}$$

(Eqn S77)

$$M_{AB} = 2 \left[\frac{1}{M_A} + \frac{1}{M_B} \right]^{-1}$$

(Eqn S78)

Isobaric conditions were established by the operation of the experimental system at atmospheric pressure i.e. negligible pressure drop across the reactor, verified by pressure gauge readings at the inlet and outlet of the reactor. The assumption that isotheral conditions exist within the axially probed region of the bulk gas phase (z = 0-60 mm) has already been shown not to be reflective of the true conditions, Fig. S2. However, the discrepancy between

real and assumed bulk gas phase temperature is minimised by using the experimentally axially measured temperature (T_g) to calculate the molecular diffusion of each gaseous component. The diffusional volumes ($\Sigma_{v,i}$) were calculated using the atomic parameters determined by Fuller *at al.*[19,20]. The atomic parameters determined by Fuller *et al.* were attained through regression analysis of various experimental studies, stating an average absolute error of 4% when used in conjunction with Eqn. S77.

Diffusion in the catalyst mesopores was expected to occur via Knudsen diffusion, therefore the process was modelled via Eqn. S79, in which D_{Kn} represents local diffusivity via Knudsen diffusion within the mesopores (m^2.s^{-1}), ε_{mes} the mesopore porosity, d$_{mes}$ the mesopore diameter (m), γ_{mes} the mesopore tortuosity, R represents universal gas constant (J.mol^{-1}.K^{-1}), T the gas temperature (K) and M$_i$ represents molecular mass of species *i* (g.mol^{-1})[10].

$$D_{kn} = \frac{\varepsilon_{mes} d_{mes}}{3\gamma_{mes}} \sqrt{\frac{8RT_g}{M_i \pi}}$$

(Eqn S79)

For cases in which the forward molecular diffusion of species A is equal to the backwards molecular diffusion of species B, effective diffusivity of species A (D$_{e,A}$) can be calculated via Eqn. S80.

$$D_{eff,A} = \left(\frac{1}{\dfrac{1}{D_{kn}} + \dfrac{1}{D_{AB}}} \right)$$

(Eqn S80)

Heat Transfer
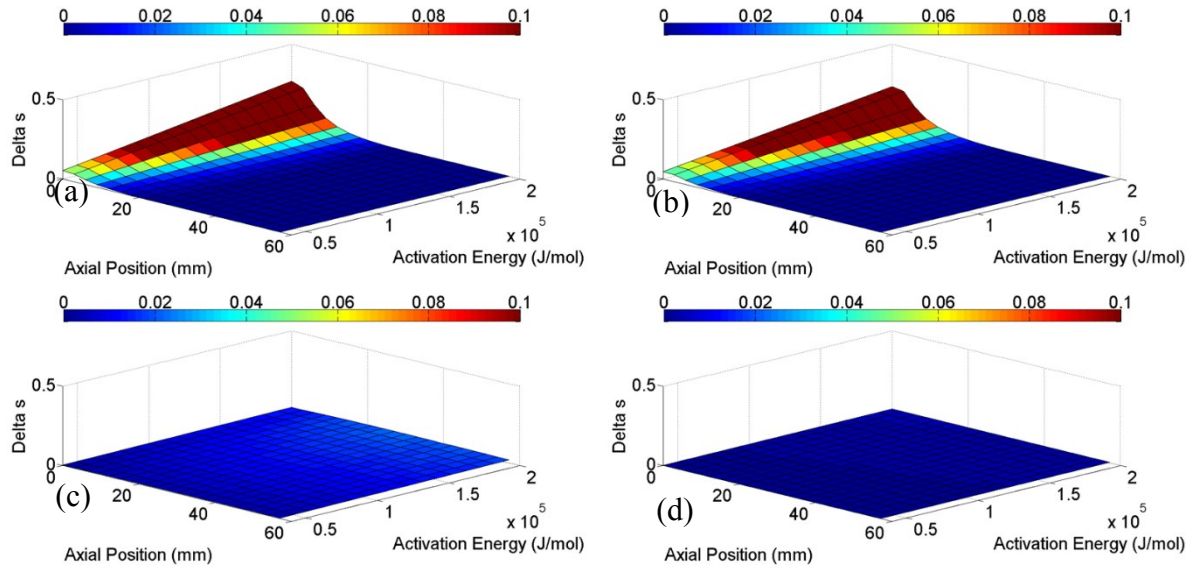
Fig. S8 Plot of δ_s as a function of axial position and activation energy for (a) 0%H_2O (b) 1%H_2O (c) 5%H_2O (d) 10%H_2O at a steady state furnace temperature of 400°C

Mathematical Fitting

The method selected to calculate the observed rate employed a purely mathematical expression in the form of a linear combination of decaying exponential functions, to represent the change in concentration with residence time, Eqn. S81.

$$C_{CH4} = a_0 + a_1 e^{-a_2 t} + a_3 e^{-a_4 t}$$ (Eqn S81)

Parameters a_0, a_1, a_2, a_3 and a_4 were estimated via Bayesian estimation using Athena Visual Studios. The first derivative $\left(\dfrac{d\,C_{A,g}}{d\,t}\right)$ was calculated analytically to give an equation of the form of Eqn. S82.

$$\frac{dC_{CH4}}{dt} = -a_1 a_2 e^{-a_2 t} - a_3 a_4 e^{-a_4 t}$$ (Eqn S82)

An example of the double exponential fitting is highlighted in Figs. S9 and S10.
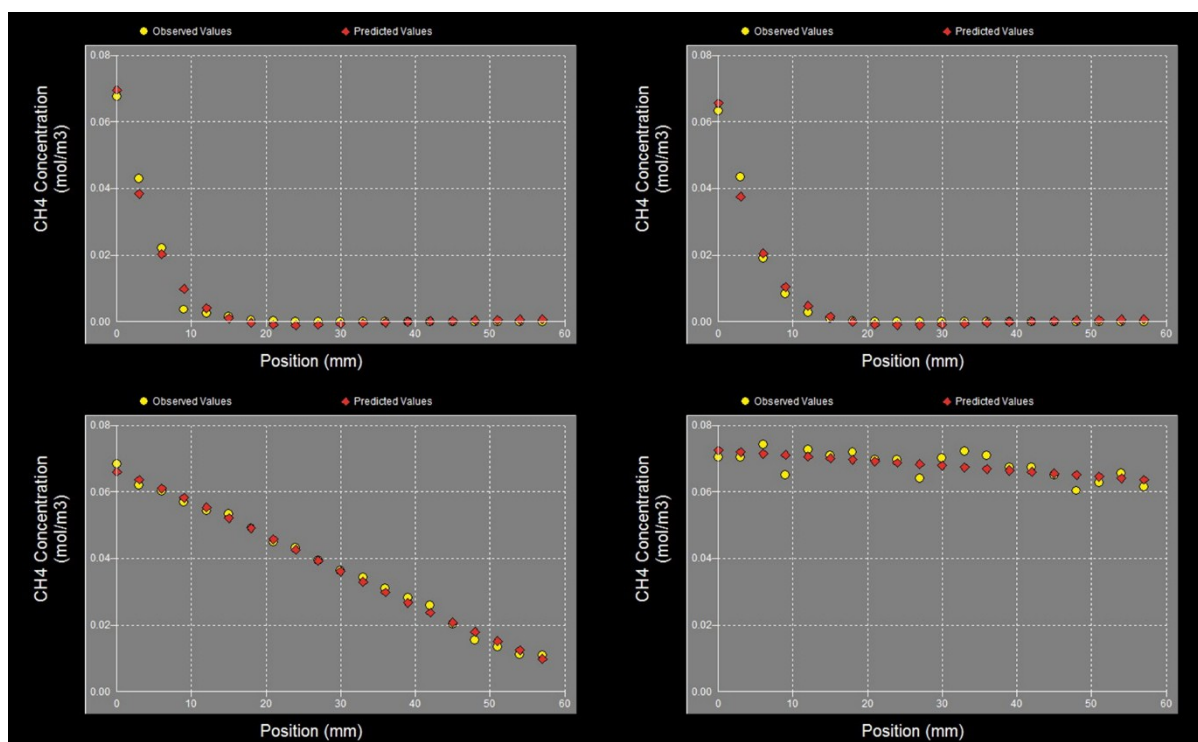
Fig S9 Double exponential fit of CH$_4$ concentration as a function of axial position for inlet H$_2$O concentrations of (a) 0% H$_2$O (b) 1% H$_2$O (c) 5% H$_2$O (d) 10% H$_2$O at a steady state furnace temperature of 400 °C.
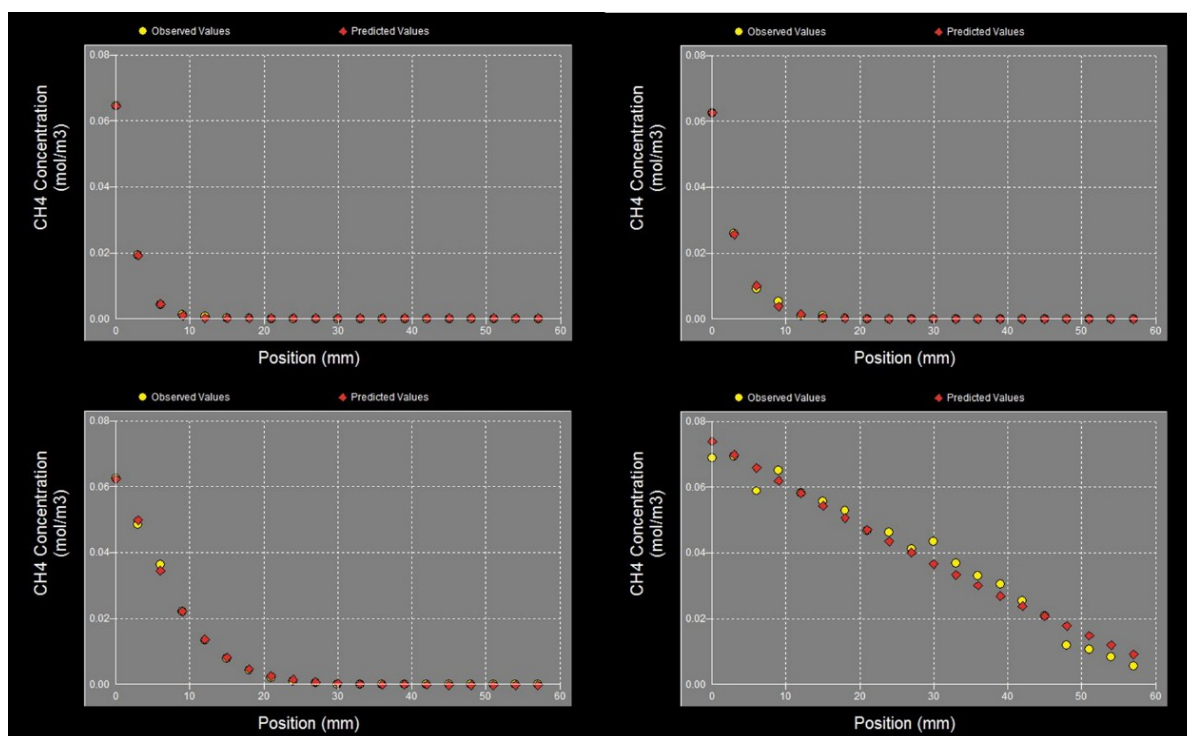
Fig. S10 Double exponential fit of CH$_4$ concentration as a function of axial position for inlet H$_2$O concentrations of (a) 0% H$_2$O (b) 1% H$_2$O (c) 5% H$_2$O (d) 10% H$_2$O at a steady state furnace temperature of 450 °C

Parameter Estimation

NLLS regression employs the total residual sum of squares as a means of delivering parameter estimates, relying solely on residual minimisation without statistical critique. In contrast, Bayesian parameter estimation provides a more robust method of parameter estimation, utilising a combination of experimental observations and prior information in conjunction with Bayes theorem, to infer a posterior distribution for the parameters of the postulated model.[11] Using the posterior distribution, it is possible to calculate the most likely parameter values for the given model, assessing the statistical significance of the parameter estimates in the process. Additionally, the 95% highest posterior density intervals (HPD) were calculated for each estimated parameter, further adding to the confidence of the parameter estimates.
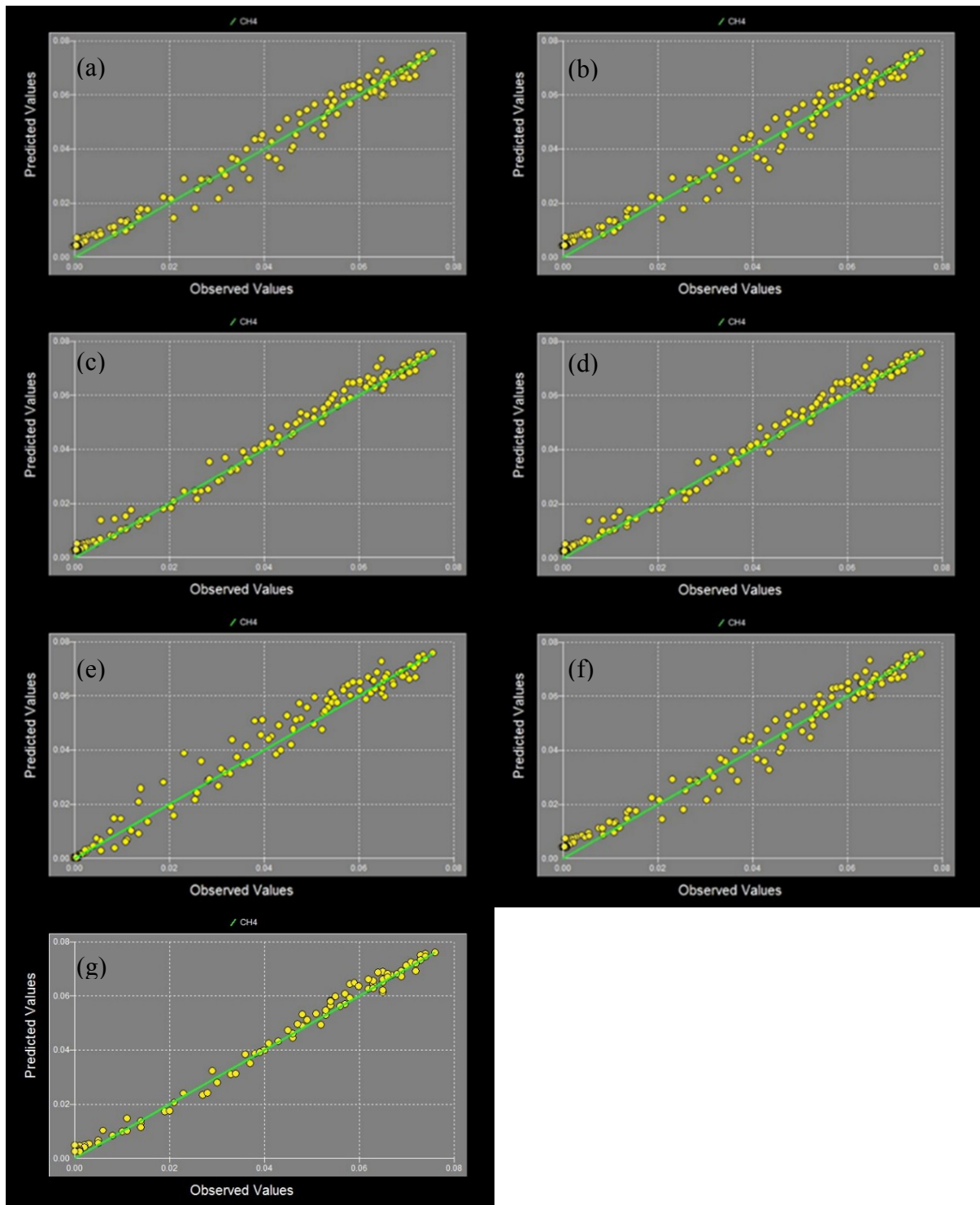
Fig. S11 Parity plots resulting from the model fitting and parameter estimation procedure performed exclusively with respect to non – mass transfer data sets in which insignificant gas – solid temperature differences were predicted (a) Model 1 (b) Model 2 (c) Model 3 (d) Model 4 (e) Model 7 (f) Model 8 (g) Model 9.

Dual Site Model Derivation

Model 9 is derived based on the assumption that two active sites exist for CH_4 oxidation, site one (S_1) representing oxidised PdO and site two (S_2) representing a hypothesised $Pd(OH)_x$ species. S_2 is thought to form from the conversion of S_1 (PdO) to $Pd(OH)_x$ in the presence of H_2O, represented by Eqn S83. In this situation, S_1 is surmised to be a more active site than S_2, with respect to the CH_4 oxidation, therefore $r_{S1} \gg r_{S2}$. The total rate of CH_4 oxidation is dictated by the sum of rates r_{S1} and r_{S2}, Eqn. S84.

$$S_1 + xH_2O \rightleftharpoons S_2 \qquad \text{(Eqn S83)}$$

$$rate = r_{S1} + r_{S2} \qquad \text{(Eqn S84)}$$

The total number of available adsorption sites is denoted by Eqn. S85, in which the surface coverage of CO_2, O_2 and CH_4 is assumed to be negligible, therefore all available sites are attributed exclusively to PdO and $Pd(OH)_x$ sites, represented in Eqn. S86 as fractions of the total available sites.

$$[S_T] = [S_1] + [S_2] \qquad \text{(Eqn S85)}$$

$$1 = \theta_1 + \theta_2 \qquad \text{(Eqn S86)}$$

The rate of CH_4 oxidation on the oxidised sites S_1, is assumed to be proportional to the partial pressure of CH_4 in the gas phase, the CH_4 oxidation rate constant k_1 and the surface coverage of oxidised sites, Eqn. S87. The rate of CH_4 oxidation on the inhibited sites S_2, is assumed to be proportional to the partial pressure of CH_4 in the gas phase, the CH_4 oxidation rate constant k_2 and the surface coverage of inhibited sites, Eqn. S88 where the rate constant $k_2 \ll k_1$.

$$r_{S1} = k_1 \theta_1 P_{CH4} \qquad \text{(Eqn S87)}$$

$$r_{S2} = k_2 \theta_2 P_{CH4} \qquad \text{(Eqn S88)}$$

The position of equilibrium with respect to Eqn. S83, is calculated via Eqn. S89, in which it is assumed that the adsorption of H_2O on site S_1 leads to the formation of site S_2.

$$K_{eq} = \frac{[S_2]}{[S_1][H_2O]^x}$$

(Eqn S89)

$$[S_2] = K_{eq}[S_1][H_2O]^x$$

(Eqn S90)

$$[S_1] = \frac{[S_T]}{1 + K_{eq}[H_2O]^x}$$

(Eqn S91)

The substitution of Eqn. S88, S89, S90 and S91 into Eqn. S84, results in the formation of Eqn. S92, describing the rate of CH_4 oxidation as a function of CH_4 and H_2O partial pressures.

$$rate = \frac{k_1 P_{CH4}}{1 + K_{eq}[H_2O]^x} + \frac{k_2 K_{eq}[H_2O]^x P_{CH4}}{1 + K_{eq}[H_2O]^x}$$

(Eqn S92)

$$r_m = \frac{k_1 C_{CH4} + K_{Eq} k_2 C_{CH4} C_{H2O}^x}{(1 + K_{Eq} C_{H2O}^x)}$$

(Eqn S93)

Variations of Model 9

Table S4 Global kinetic rate expressions of Model 9, with x = 1,2 and 3 for H_2O^x

Model	Rate Expression	X = 1, 2, 3 (Eqn S92)
9 (a)	$$r_m = \frac{k_1 C_{CH4} + K_{Eq} k_2 C_{CH4} C_{H2O}}{(1 + K_{Eq} C_{H2O})}$$	1
9 (b)	$$r_m = \frac{k_1 C_{CH4} + K_{Eq} k_2 C_{CH4} C_{H2O}^2}{(1 + K_{Eq} C_{H2O}^2)}$$	2
9 (c)	$$r_m = \frac{k_1 C_{CH4} + K_{Eq} k_2 C_{CH4} C_{H2O}^3}{(1 + K_{Eq} C_{H2O}^3)}$$	3
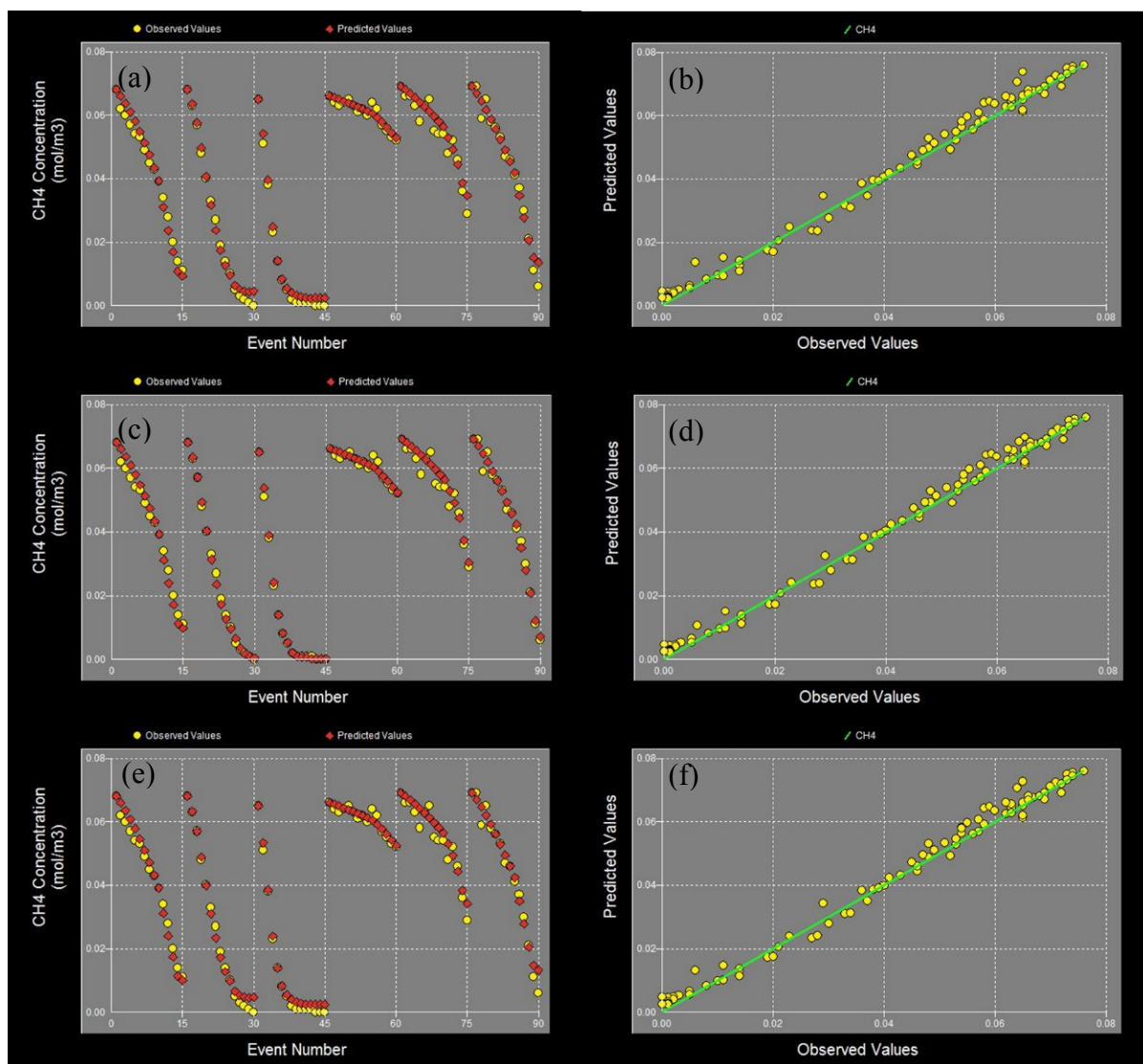
Fig. S12 Experimental and simulated CH$_4$ concentration as a function of event number (EN) for (a) Model 9 *(a)*, (c) Model 9 *(b)* and (e) Model 9 *(c)*. under feed conditions of 4000 ppm CH$_4$, 12% O$_2$, balance Ar and H$_2$O concentrations of 5 and 10 vol%, and utilising steady state furnace temperatures of 400 – 450 ºC.

Exemplar Experimental Error

An axial resolution of 0.1 mm ±5% was possible when employing of the Thorlabs APT Microstepping Controller (BSC101). However, the main potential for errors in the axial direction originated from the initial probe alignment to the front of the monolith during the reactor setup step. During this step, the probes were visually aligned to the inlet face of the monolith core using the Thorlabs APT software. The probes were translated through the full axial experimental range (60 mm), followed by 60 mm translation in the reverse direction to

return the probes to the inlet of the monolith. This process was repeated three times, each time assessing the deviation of the inlet probe position from its initial position at the inlet. From the deviation measurements, it was determined that an error of approximately 0.5 mm was sufficient to account for the axial positioning error.

In terms of the experimental error in the y-axis (CH_4 concentration), each position averaged CH_4 concentration value was assumed to exhibit an error equal to one standard deviation of the 138 data points used to calculate it. At lower CH_4 concentration values, the potential error was elevated due to the decreased signal to noise ratio, see Figure S13.
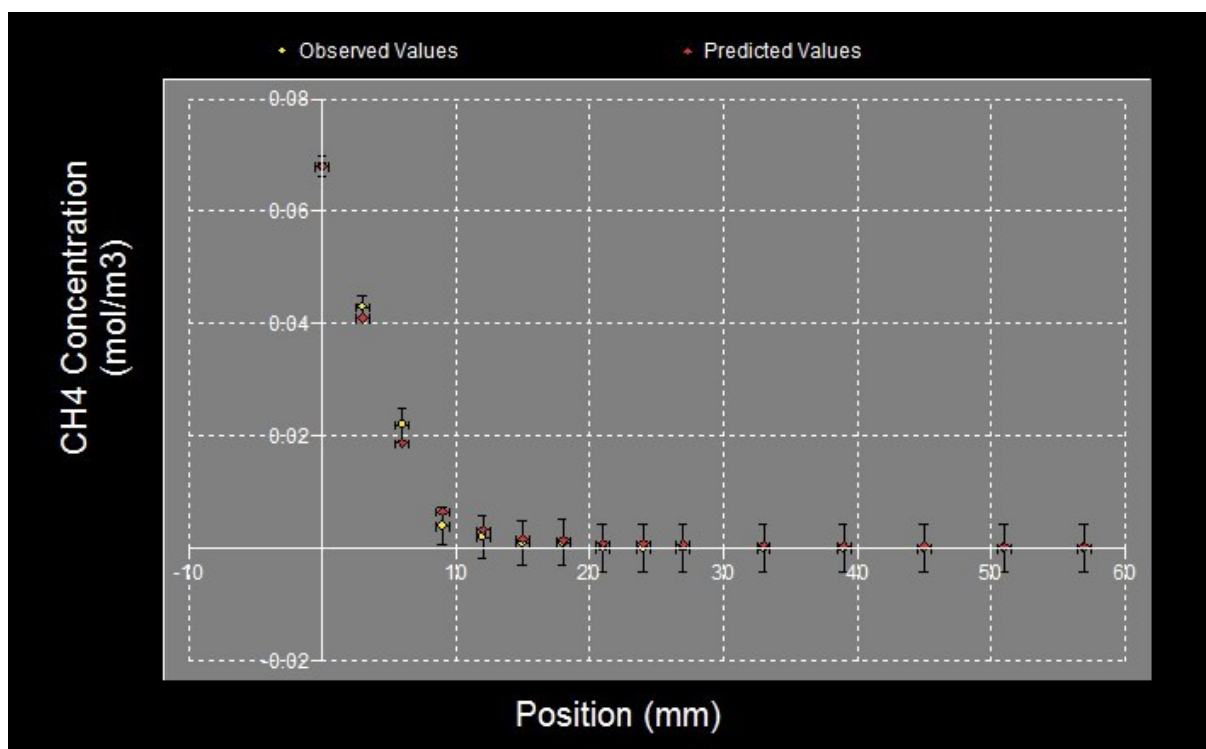
Fig. S13 Example of potential experimental errors associated with observed CH_4 concentration during the reaction employing feed conditions of 4000 ppm CH_4, 12% O_2, balance Ar and 0 v/v% H_2O concentrations, utilising a steady state furnace temperature of 400 ºC.

(1) A.F. Ahlstrom-Silversand, C.U.I. Odenbrand, *Appl. Catal. A*, 1997, **153**, 157.

(2) J.C. Van Giezen, F.R. Van Den Berg, J.L. Kleinen, A.J. Van Dillen, J.W. Geus, *Catal. Today*, 1999, **47**, 287.

(3) R. Burch, F.J. Urbano, P.K. Loader, *Appl. Catal.*, 1995, **123**, 173.

(4) F.H. Ribeiro, M. Chow, R.A. Dalla Betta, *J. Catal.*, 1994, **146**, 537.

(5) R.G. Shahrestani, *Kinetic and Deactivation Studies of Methane Oxidation over Palladium Catalysts in the Presence of Water*, PhD Thesis, The University of British Columbia, Vancouver, 2015.

(6) G. Groppi, A. Belloli, E. Tronconi, P. Forzatti, *Chem. Eng. Sci.*, 1995, **50**, 2705.

(7) D.E. Mears, *Ind. Eng. Chem. Process Des. Dev.*, 1971, **10**, 541.

(8) E.N. Fuller, K. Ensley, J.C. Giddings, *J. Phys. Chem.*, 1969, **73**, 3679.

(9) B.E. Poling, J.M. Prausnitz, J.P. O'Connel, *The Properties of Gases and Liquids*, McGraw-Hill, New York, USA 2001.

(10) V. Novak, P Koci, M. Marek, F. Stepanek, P. Blanco-Garcia, G. Jones, *Catal. Today*, 2012, **188**, 62.

(11) W.E. Stewart, M. Caracotsios, *Computer-aided Modelling of Reactive Systems*, John Wiley & Sons, Inc. Hoboken, New Jersey, USA, 2008.